ARTICLE

Graphene Oxide and Low-Density Polyethylene Based Highly Sensitive Biomimetic Soft Actuators Powered by Multiple Clean Energies of Humidity and Light

Received 00th January 20xx,
Accepted 00th January 20xx

DOI: 10.1039/x0xx00000x

Yiwei Zhang,[abc] Ruiqian Wang,[abc] Wenjun Tan,[abc] Lianchao Yang,[abc] Xiaolong Lv, [ab] Xiaodong Wang,[abc] Feifei Wang,[d] Chuang Zhang[ab*]

Soft actuators based on smart response materials can utilize external stimuli, especially clean energy sources such as light and humidity found in nature, to achieve controllable actuation and perception, which has attracted much attention in the development of smart robots. However, most existing soft actuators based on light or humidity stimulation may suffer from several shortcomings, such as low response sensitivity, a single response mode, and an inability to achieve a multi-stimulus cooperative response. Hence, inspired by the biological structure of plants, we have fabricated soft double-layer actuators with ultrahigh sensitivity by casting a graphene oxide (GO) solution on a low-density polyethylene (LDPE) film. With just 40 mW cm^{-2} of NIR light, the actuator can quickly change from the curled state to the flat state, achieving an angle change of 500°, which is less than the natural light intensity (80 mW cm^{-2}). Moreover, the actuator also showed a rapid response (~2.6 s) and large deformation (500°) under humidity stimulation. As an application concept demonstration, the actuator can be assembled into a crawling robot that mimics inchworms crawling on a leaf, an adaptive soft gripper that grabs different shapes of cargo, and a rotating robot driving a boat forward. The soft actuator will have great potential in smart bionics, energy conversion, and other emerging fields in the future. future

1. Introduction

Soft robots have the characteristics of light weight, excellent impact resistance, flexibility, continuous deformation, etc., which enable them to have higher sensitivity, wider applicability, and intrinsic safety, hence possessing significant development potential in emerging fields such as environmental monitoring, intelligent bionics, and human–computer interaction[1–4]. In particular, a soft actuator, as the core of a soft robot, plays a decisive role in the performance of the robot.

The actuated deformation capability of soft actuators is mainly dependent on the smart response materials. These smart materials can translate different external stimuli, such as humidity[5,6], light[7,8], temperature[9,10], pH[11], solvent[12], electricity[13–16], and magnetism[17–19], into specific displacement and force, allowing smart actuators to mimic natural creatures' behaviors, such as crawling[5,20], grabbing[21,22], flying[23,24], and swimming [13,25,26]. However, among the various types of stimuli, smart materials responding to electricity, pH, solvent, magnetism, and other stimuli types have limited application scenarios due to high energy consumption, harsh usage conditions, and the need for manual intervention or complex systems, all of which are not conducive to environmental protection, resource savings, and sustainable development[27–29]. At the same time, nature provides a potential research method for the development of smart responsive materials. Sunlight and water (humidity) are abundant and ubiquitous in nature[30,31]. Through eons of evolution, some organisms have evolved tissues or organs that respond to sunlight or water to better sustain their survival and reproduction, such as phototropic growth and photosynthesis in plants[32,33] and morphological changes in pinecone scales and wheat awns under wet and dry conditions (Fig. 1(a))[34–37]. These stimuli in nature are ideal and sustainable energy sources for the development of soft actuators based on smart responsive materials.

Therefore, by mimicking the structure of certain natural organisms, researchers have developed a wide variety of smart materials and related actuators to utilize the energy contained in light and humidity. For example, inspired by shape transformation stimulated by plants under a change in humidity, FengGong et al. developed a biomimetic soft actuator composed of PEO for shape transformation and PVDF for power generation; the soft actuator can generate electricity when exposed to breath, wet paper, and hot water and steam generated by a solar evaporator and could then power electronic devices through rectification and storage[38]. Beomjune Shin et al. used the alignment of directional electrostatic spinning to produce a nanometer fiber moisture response from the membrane; the membrane responds to humidity changes by rapidly expanding and contracting vertically[5].

[a] State Key Laboratory of Robotics, Shenyang Institute of Automation, Chinese Academy of Sciences, Shenyang, 110016, China.
[b] Institutes for Robotics and Intelligent Manufacturing, Chinese Academy of Sciences, Shenyang 110169, China
[c] University of Chinese Academy of Sciences, Beijing 100049, China.
[d] Department of Electrical and Electronic Engineering, The University of Hong Kong, Hong Kong 999077, Hong Kong.

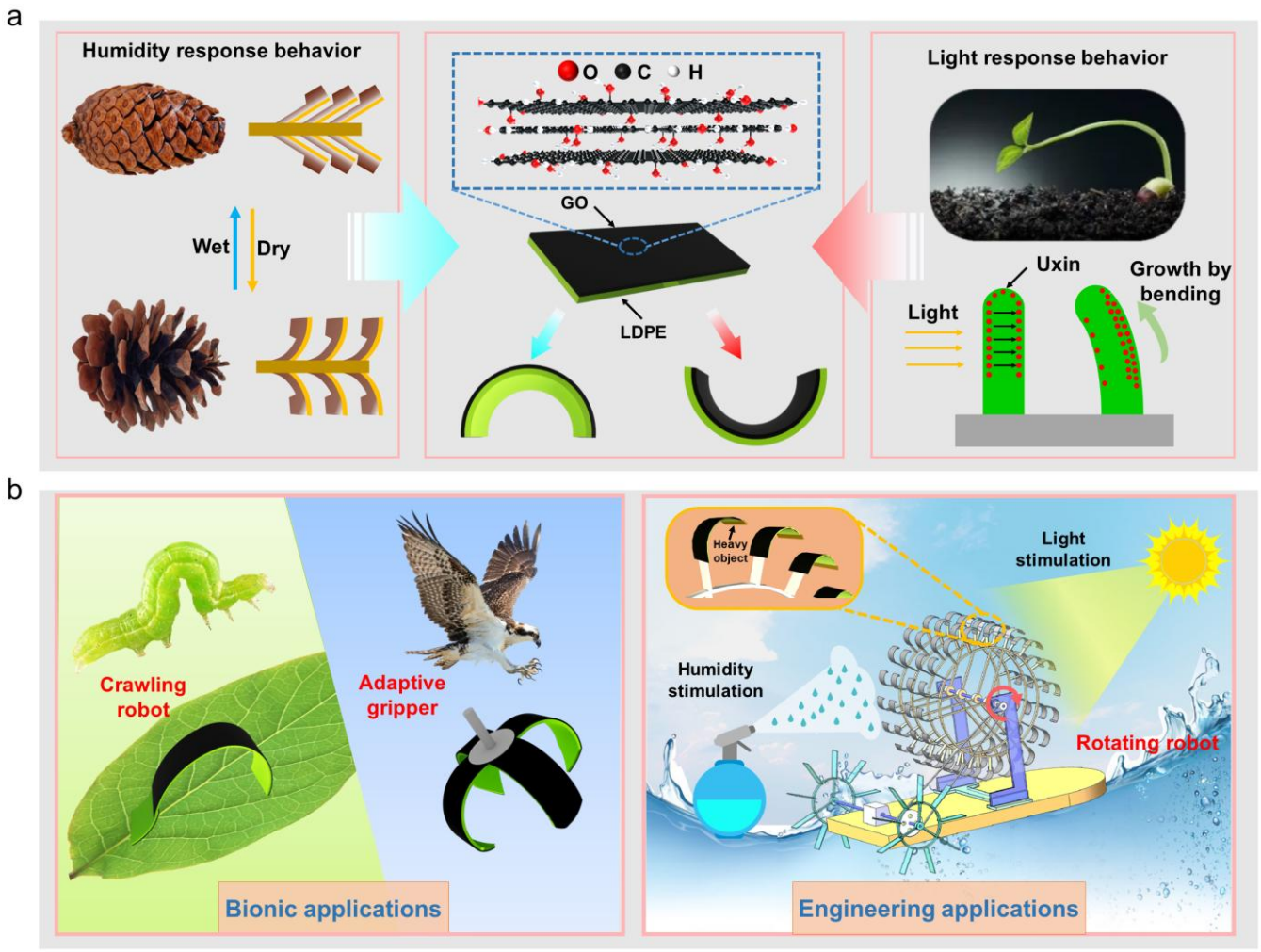

Fig. 1. (a) Biological structures-inspired GO/LDPE actuator is capable of using light and humidity to achieve bending motion. (b) Applications of the GO/LDPE actuator: inchworm-inspired crawling robot, hawk claw-inspired adaptive soft gripper, and the rotating robot.

Ying et al. made inchworm soft robots based on asymmetric layered microstructures with dual piezoelectric actuators by grafting coupling agents into MXene nanosheets, which were able to realize directional motion using natural light[39]. Yue et al. microstamped a hydrogel onto a GO film to fabricate a multi-responsive actuator with precise patterns; the programmable actuator can respond to multiple stimuli, such as humidity, temperature, and light, and can grasp, crawl, and wrap like creatures in nature[40]. Although the actuators reported in the previous literature have excellent performance, there may be other shortcomings to overcome, including the need for strong stimulation, lower sensitivity, a single response mode, or the inability to achieve a multi-stimulus cooperative response. On the one hand, changes in light and humidity in the natural environment are slow and weak; hence, it is necessary to develop multi-responsive actuators with high sensitivity to meet the application requirements of a real environment. On the other hand, it is also crucial to develop suitable real applications under natural conditions. Light and humidity changes caused by water evaporation occur at almost the same time. Nevertheless, most of the current research and application scenarios only aim at a single stimulus, which cannot achieve multi-stimulus synergistic responses and cannot make full use of energy in light and humidity. Therefore, how to develop multi-responsive actuators with high sensitivity that use synergistic stimulation of light and humidity to accomplish specific tasks has become a serious challenge.

To solve the above challenges, we need to choose suitable materials to make multi-responsive actuators and design reasonable structures and control methods to drive robots. In terms of material selection, GO and LDPE materials are used. GO, one of the most important graphene derivatives, has been demonstrated to be an outstanding candidate for the construction of intelligent and high-performance GO-based bilayer actuators. This is due to its many attractive properties, such as excellent flexibility, low density, good stability, large surface area, humidity-sensitive characteristics, high light-to-heat conversion efficiency, and thermal conductivity.[41, 42] In addition, achieving sensitive photothermal actuation requires excellent thermal expansion materials. Common thermal expansion materials are hydrogels [43–45], shape-memory liquid crystal materials[46–48], and various high-polymer plastics[49,50]. Among them, LDPE film, with a huge coefficient of thermal expansion (CTE) of up to 400×10^{-6} °C^{-1}, has become an excellent material for fabricating photothermal response actuators[51]. Regarding structural design and control methods, we designed inchworm structures, claw structures, and rotary structures and controlled soft robot motion through single or multiple stimuli.

Here, inspired by the response properties of the bilayer structure in plant tissue, we prepared a biomimetic bilayer soft actuator composed of GO and LDPE using the oxygen plasma technique and the solvent evaporation method. The abundant oxygen-containing functional groups, the photothermal conversion characteristics of GO, and the huge CTE difference between GO and LDPE give the actuator excellent humidity and photothermal actuation performance. With just 40 mW cm^{-2} of NIR light, the actuator can quickly go from a curled state to a flat state, with an angle change of 500°, showing the ultrahigh light response sensitivity of the soft actuator. Meanwhile, the actuator also has a strong humidity response with an angle change of 500° in a high-humidity environment. In addition, as application concepts, an inchworm-inspired crawling robot, an adaptive soft gripper, and a rotating robot were fabricated to demonstrate the actuator's excellent performance (Fig. 1(b)). Inchworm-inspired crawling robots can achieve directional crawling on leaves under the control of NIR light; the adaptive soft gripper can grab, move, and release objects of different shapes under the sequential control of humidity and NIR light. The rotating robot can be synergistically stimulated by humidity and light to rotate rapidly to drive a boat forward. Therefore, biomimetic soft actuators will have huge development potential in soft robots, artificial muscles, smart sensors, energy conversion equipment, and other fields in the future.

2. Results and discussion

2.1 Fabrication and structural characterization of the GO/LDPE bilayer actuators

The multi-response-driven GO/LDPE composite film was fabricated by simple solution evaporation, as illustrated in Fig. S1. First, the LDPE film cut into a fixed size was treated in oxygen plasma for five minutes to obtain a film with surface hydrophilic properties. Then, the film was fixed by tape to the bottom of a petri dish before casting the GO solution on top of it and allowing it to dry naturally under a fume hood. Finally, a GO/LDPE actuator was obtained by peeling off the composite film from the petri dish. Fig. 2(a) shows a cross-sectional structure of the GO/LDPE film. Due to the hydrophilic treatment of the LDPE surface using oxygen plasma technology, the two-layer structure can be tightly contacted. GO presents a layered structure (Fig. 2(b)). Fig. 2(c) shows the surface SEM of the GO layer. In the microscopic state, GO has a rough surface, which may be conducive to the absorption and excitation of water molecules.

In addition, the elemental distributions of GO and LDPE were measured by elemental analysis instruments. Oxygen and carbon are the main components of GO (Fig. S2(a, b)). Sulfur was also detected,

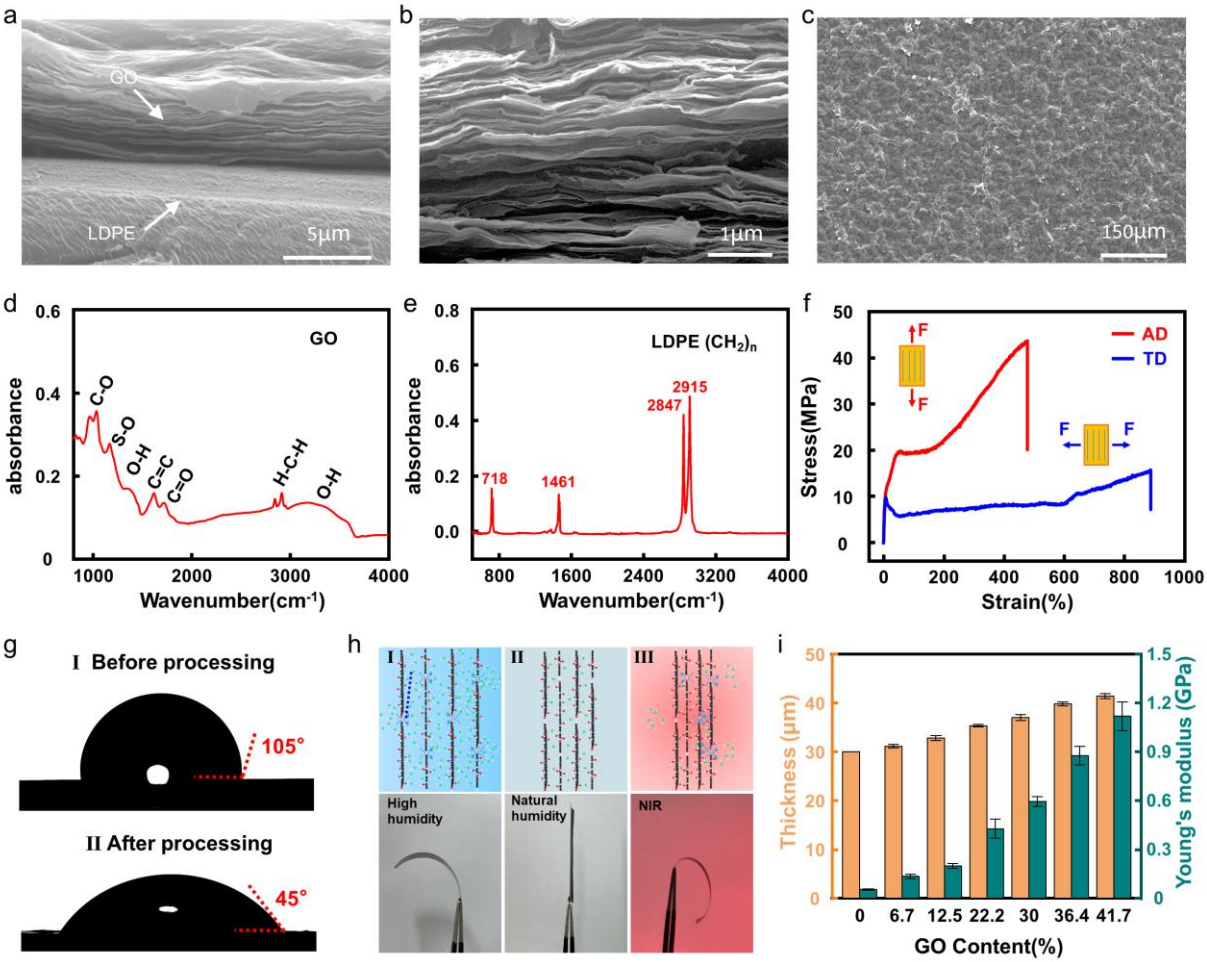

Fig. 2. (a) Cross-sectional SEM image of the GO/LDPE actuator. (b) Layered structure SEM image of GO cross-section. (c) Surface SEM image of GO layer. (d) FTIR spectroscopy of GO. (e) FTIR spectroscopy of LDPE. (f) Stress–strain curves of LDPE. (g) Contact angles of LDPE film before and after processing. (h) Schematic diagram of GO layer response to high humidity and NIR light. (i) Thickness and Young's modulus of the actuator with different GO content.

which was due to the sulfate group of sodium dodecyl sulfate (SDS) (Fig. S2(c)). Fig. S2(d) shows the carbon element distribution of LDPE. Fig. 2(d) shows the Fourier-transform Infrared Spectroscopy (FTIR) of GO with absorption peaks for multiple functional groups[52, 53], including the OH stretching vibration peak located at 3300-3500 cm^{-1}, C=O stretching vibration peak near 1726 cm^{-1}, C=C stretching vibration absorption peak near 1620 cm^{-1}, bending vibration of O-H at 1380 cm^{-1}, and C-O stretching vibration peak at approximately 1040 cm^{-1}. In addition, it can be observed from Fig. 2(d) that the asymmetric stretch vibration peak and the symmetric stretch vibration peak of CH_2 appear at 2920 cm^{-1} and 2850 cm^{-1}, respectively, and the stretching vibration peak of S-O is located near 1146 cm^{-1}, which is due to the addition of the surfactant SDS when making the GO solution [54]. LDPE mainly contains one kind of group -CH_2. As shown in Fig. 2e, there are four absorption peaks in the FTIR spectra of LDPE, which are the asymmetric and symmetric stretching vibration peaks near 2915 cm^{-1} and 2846 cm^{-1}, the bending vibration peak near 1459 cm^{-1}, and the rocking vibration peak near 718 cm^{-1} [55]. In addition, we measured the mechanical properties of LDPE. LDPE is anisotropic due to directional crystallization[50]. The fracture stress in the alignment direction (AD) is greater than that in the transverse direction (TD), while the elongation at break is just the opposite (Fig. 2(f)).

Before fabrication of the GO/LDPE actuator, the LDPE films were treated with oxygen plasma technology. Before oxygen plasma treatment, the LDPE film is hydrophobic, with a contact angle of 105°. After treatment, the contact angle drops to 45°, and the LDPE film becomes hydrophilic for better attachment with GO, enhancing the mechanical strength of the film (Fig. 2(g)). Fig. 2(h) shows the schematic models and optical photos of the actuator excited by NIR light and humidity. When the actuator is excited by humidity, the GO layer and LDPE layer are the water absorption active layer and inert layer, respectively, which induce a water expansion difference and lead to the bending of the film toward the LDPE side. When irradiated by NIR light, the GO layer and LDPE layer are the negative thermal expansion layer and thermal expansion layer, respectively. The photothermal conversion of GO causes the LDPE layer to expand and bend toward the GO layer, accompanied by the desorption of water molecules. Notably, GO/LDPE films of different thicknesses can be obtained by controlling the volume of the added GO solution. To obtain the best material parameters of the GO/LDPE actuators, six actuators with different GO contents were fabricated, where the LDPE layer was fixed at 30 μm in thickness. The GO content is positively correlated with the thickness and Young's modulus of the actuator (Fig. 2(i)).

Furthermore, in the production process, since the shrinkage of GO during drying causes uneven stress distribution on the surface of the LDPE film, the peeled composite film will generally produce irregular bending with the LDPE layer toward the outside, as shown in Fig. S3. To obtain an actuator with good bending direction consistency, thermal adjustment of the film is needed. The GO/LDPE film was cut into a rectangle of 10 mm×30 mm. Then, the GO/LDPE film was held on both sides using the slide to keep it flat and placed on the heating plate for thermal adjustment treatment (Fig. S4). In the heating process, the thermal expansion of LDPE will cause the GO sheet to slide. After cooling, the LDPE layer of the driver will shrink, but the slip of the GO sheet generated during the thermal regulation stage cannot be fully recovered during the cooling stage[50, 56]. As a result, the heat-treated GO/LDPE actuator finally presents a curly state with the GO wrapped around it. By controlling the heating temperature and time, different bending angles of the film can be obtained (Fig. S5).

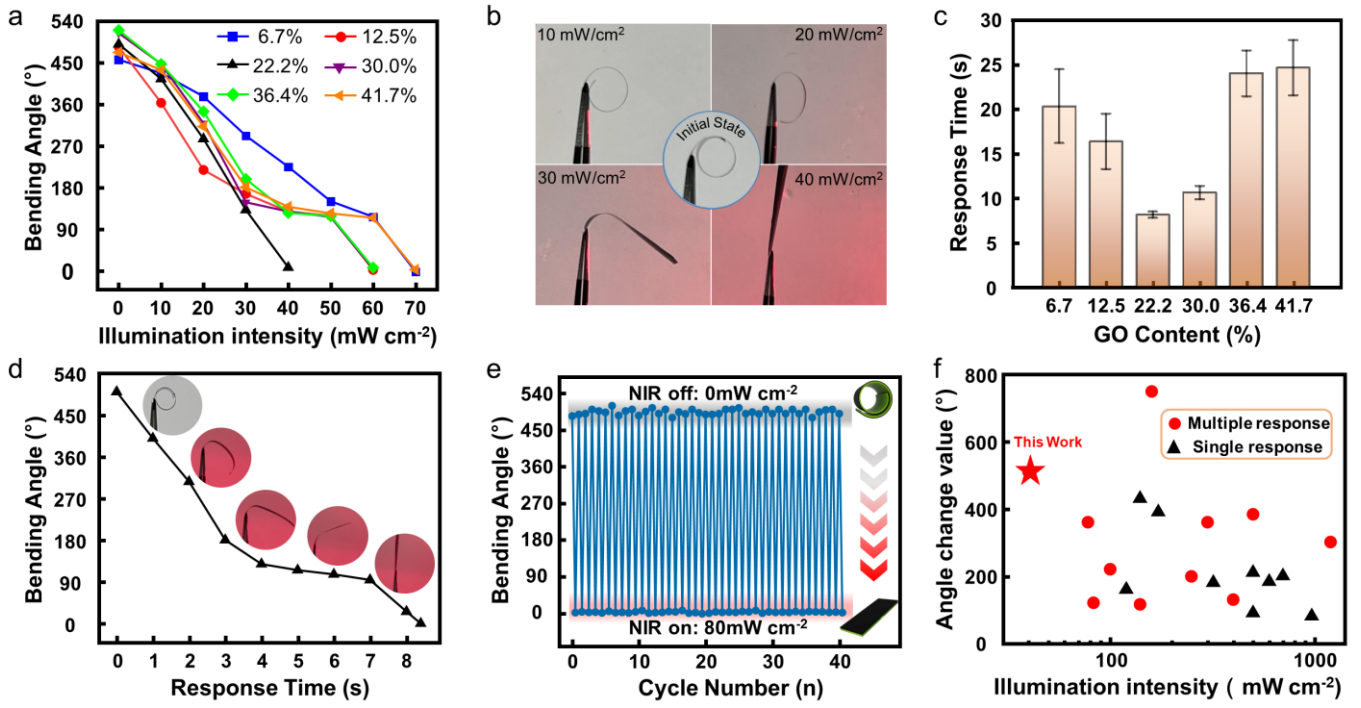

Fig. 3. NIR actuation performance of GO/LDPE actuators. (a) Bending angle as a function of NIR intensity with different GO content of the GO/LDPE actuator. (b) Optical photographs of the GO/LDPE actuator based on 22.2% GO at different NIR light intensities. (c) Relationship of GO/LDPE actuator response time with GO content at an illumination intensity of 80 mW cm^{-2}. (d) Bending angle of the actuator based on 22.2% GO as a function of time under an illumination intensity of 80 mW cm^{-2}. (e) NIR repeatability test of the actuator with 22.2% GO content. (f) Actuators reported in the literature compared to the GO/LDPE in this work.

Therefore, GO/LDPE film can be thermally programmed to assemble actuators or robots with different structures, functions, and uses.

2.2 Light actuating performance of GO/LDPE actuators

Due to the great CTE difference between LDPE and GO materials and the excellent photothermal conversion characteristics of GO, the GO/LDPE actuator shows an ultrafast sensitive response to NIR light. To further investigate the photosensitive response of the actuator, a typical rectangle (10 mm×30 mm) was chosen, and the initial bending angle of the six actuators was maintained at approximately 500° with the GO layer on the outside by heating adjustment. When illuminated by NIR light, the actuators open rapidly to a flat state due to the stress mismatch of the film caused by the different expansion amplitudes of the bilayer material.

The different GO contents of the film will affect the sensitivity of the actuator to the light response (Fig. 3(a)). With an increase in the GO content from 6.7%, the sensitivity of the actuator is significantly improved. When the GO content is 22.2%, the sensitivity of the actuator reaches the highest level, the angle changes to 500°, and it achieves a flat state under 40 mW cm^{-2} of light intensity. However, as the GO content continued to increase, the sensitivity of the actuator began to decline. This phenomenon may be caused by the increased rigidity of the actuator due to the thicker GO layer. Fig. 3(b) illustrates the bending response of the actuator based on 22.2% GO content under different NIR light intensities. Fig. 3(c) shows the response times of GO/LDPE actuators To fully ensure that all actuators can recover from the curled state to the flat state, we chose an illumination intensity of 80 mW cm^{-2}. Similar to the sensitivity of the actuators, the response time of the actuator decreased first and then increased with the change in GO content, reaching a minimum value of ~8 s when the GO content was 22.2%. Therefore, in the comprehensive comparison of the six actuators, the actuator based on 22.2% GO content had the highest sensitivity and fastest response speed.

Fig. 3(d) characterizes the bending angle of the GO-22.2/LDPE actuator as a function of time under the stimulus of NIR light with an intensity of 80 W cm^{-2}. In particular, when the angle of the actuator is reduced to approximately 90°, the unfolding speed is significantly slower. The situation may be caused by the actuator bending angle being parallel to the angle of NIR light irradiation at this moment, resulting in a reduction in the illumination area. Fig. 3(e) shows 40 actuation cycles of the GO/LDPE actuator switching between curled and flattened states. The bending angle has no significant differences during the cycle test, which indicates that the actuator has good reversibility and repeatability. In addition, for the microstructure characterization of the GO/LDPE actuator after the cycle test, the GO is still tightly stacked on the LDPE and does not produce obvious separation (Fig. S6), proving that the actuator possesses good stability and durability. After comparing the performance of actuators in different studies, the actuator in this work shows a more sensitive light response (Fig. 3(f), Tab. S1) In addition, the light intensity required for the GO/LDPE actuator to fully deploy is lower than the natural light intensity of 80 mW cm^{-2} [39], allowing the actuator to effectively move in natural light.

2.3 Humidity actuation performance of GO/LDPE actuators

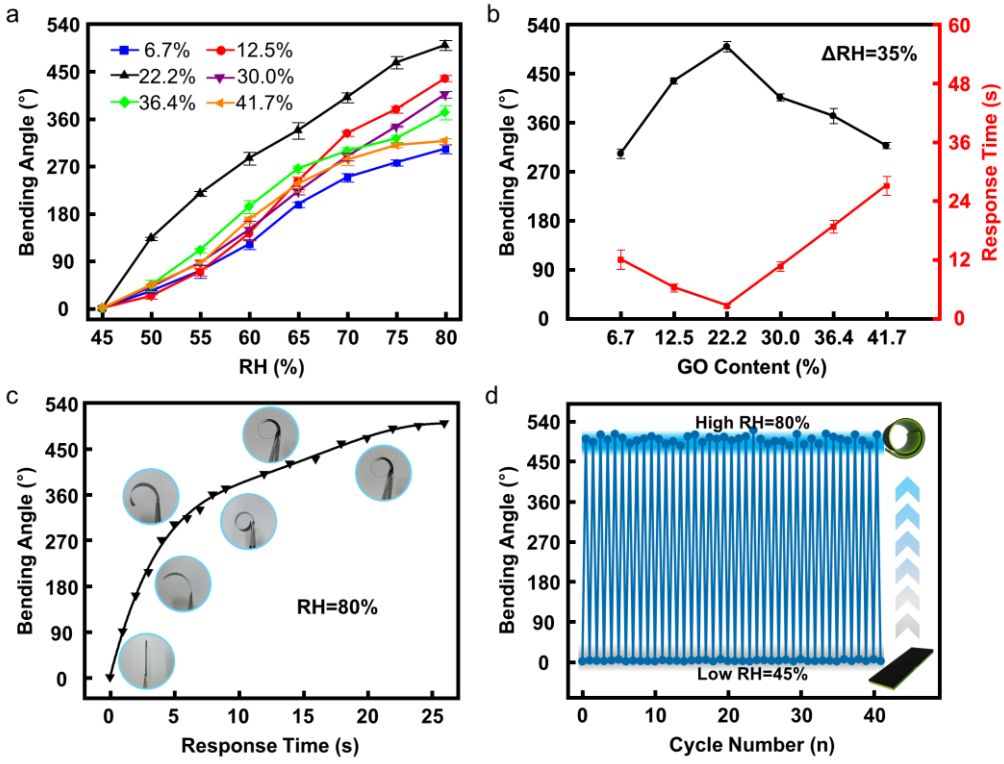

Fig. 4. Humidity actuation performance of GO/LDPE actuators. (a) Bending angle as a function of RH with different GO content of the GO/LDPE actuator. (b) Under 80% RH, the maximum bending angle of the six actuators with the GO content (black line) and the response time required for the actuators to bend to 180° (red line). (c) Under 80% RH, the bending angle of the GO-22.2/LDPE actuator as a function of time. (d) Humidity repeatability test of the GO-22.2/LDPE actuator.

The micron-level layered structure and abundant hydrophilic groups of GO allow water molecules to be dynamically inserted into the GO structure at the micro level, thus increasing the distance between the GO sheets[57], which is manifested as water absorption and expansion at the macro level. Therefore, the actuator is also able to trigger bending excitation by changing humidity conditions. Under high humidity, the hygroscopic expansion characteristics of GO and the humidity inertia of LDPE will lead to a stress mismatch of the double-layer material, resulting in asymmetric deformation of the film, which bends toward the LDPE side.

For statistical purposes, all GO/LDPE actuators were thermally adjusted, with the initial angle set near 0°. Fig. 4(a) shows the response characteristics of actuators based on different GO contents at a relative humidity (RH) of 45% to 80%. Among these six actuators, the GO-22.2/LDPE actuator exhibited the best actuating performance, and its bending angle increased rapidly from 0° to 500° with increasing RH from 45% to 80%. For the GO-6.7/LDPE actuator and GO-12.5/LDPE actuator, the GO layer is so thin that the water-adsorption-induced expansion force cannot bend the LDPE layer quickly, so the bending angle change is small in the given RH range.

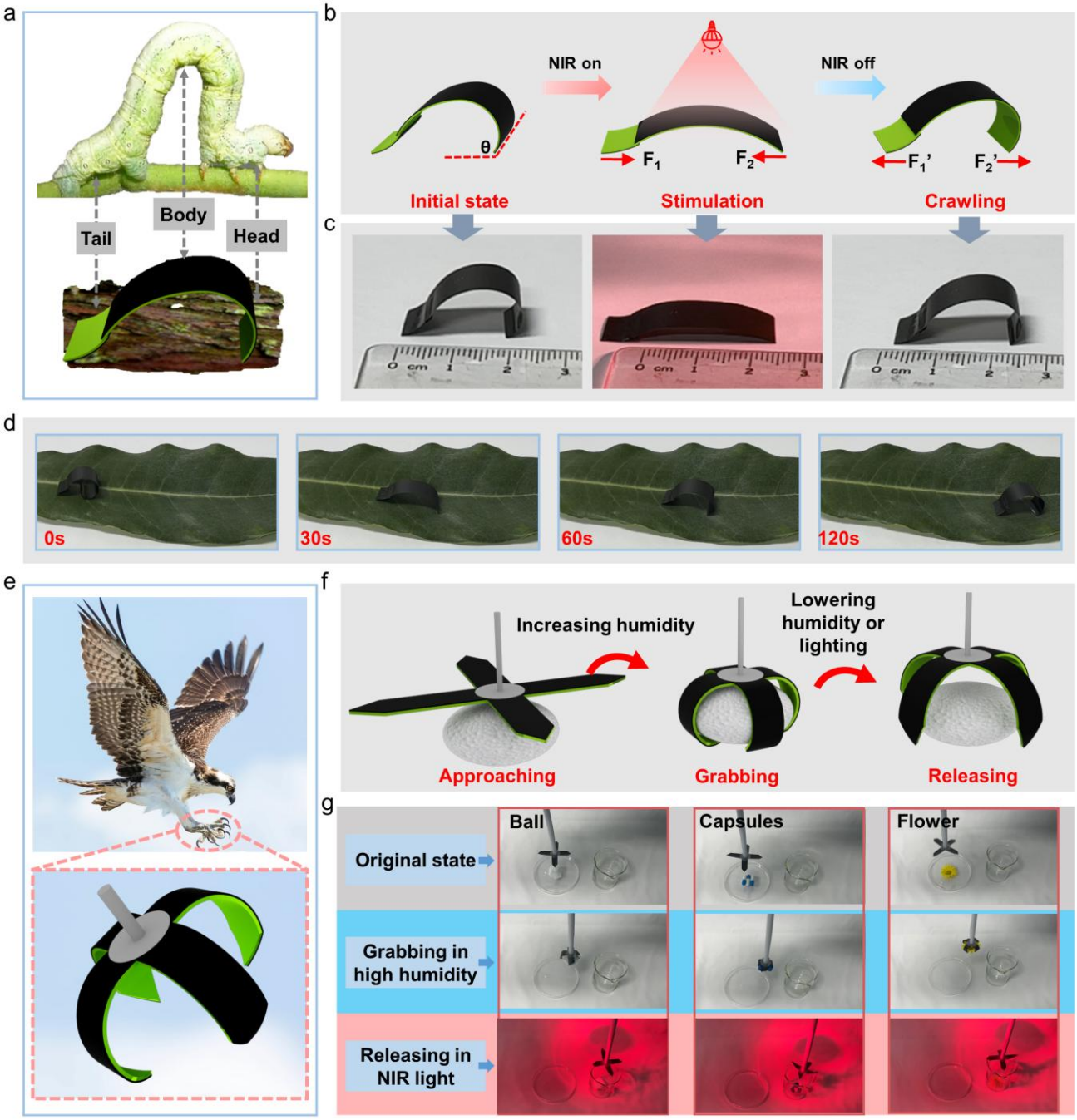

Fig. 5. Applications of GO/LDPE actuators. (a) Inchworm-inspired soft crawling robot. (b) Kinematic process analysis of a crawling robot. (c) Optical photograph of a crawling robot during one movement cycle. (d) Simulation experiment: the inchworm-inspired soft robot crawling on a leaf. (e) Hawk claw–inspired adaptive biomimetic gripper. (f) Grasping model of adaptive biomimetic gripper. (g) Grasping experiment of adaptive biomimetic gripper: ball, capsule, and flower.

For the GO-30/LDPE actuator, GO-36.4/LDPE actuator, and GO-41.7/LDPE actuator, the large stiffness of the GO layer with a large thickness means that it is difficult to bend flexibly, so the change in bending angle is less than that of the GO-22.2/LDPE actuator. In addition, to select the actuator with the best performance, we comprehensively compared the maximum bending angle and the response time of the actuator bending 180° at high humidity. As shown in Fig. 4(b), the GO/LDPE actuator has a larger bending angle (~500°) and a shorter response time (~2.6 s) when the GO content is 22.2%. Hence, we plotted the bending angle of the GO-22.2/LDPE actuator as a function of time (Fig. 4(c)). In ~7 s, the GO-22.2/LDPE actuator quickly bends from 0° to 360°; however, over the next few seconds, the actuator slows down and finally bends to its maximum angle (~500°) at 26 s. This may be due to increased internal stress and friction interference between the inner and outer layers of the actuator. In addition, under humidity stimulation, the bending and recovery process of the actuator is reversible and repeatable (Fig. 4(d)).

In addition, we have summarized recent actuators reported in the literature, including actuators that respond to humidity or light alone, as well as actuators with multiple responses (Tab. S1). As shown in Fig. S7(a), the GO/LDPE actuator possesses relatively good humidity response characteristics and may achieve relatively large deformation under small humidity changes. Although its humidity response characteristics are not optimal, the soft actuator we designed has multiple response characteristics and show extremely high light sensitivity. Compared with other actuators with multiple response characteristics, the performance of the GO/LDPE actuator is relatively excellent (Fig. S7(b)), which can achieve a light response speed of 110°/s and a humidity response speed of 69.2°/s (Fig. S7(c)).

2.4 Applications of the GO/LDPE actuator

Through a comprehensive comparison of light stimulation and humidity stimulation characterization, the GO-22.2/LDPE actuator has the best response performance. Several suitable applications can be designed to explore their potential in soft biomimetics, flexible actuation, and other fields. Many animals in nature have excellent locomotion ability, which provides strong support for the bionics of soft robots. Obviously, the inchworm is a significant biomimetic object in soft robots. The movement pattern of an inchworm is simple and divided into two main stages. First, the forefoot of the inchworm hugs the branch tightly, and the back of the body contracts and moves forward. Then, the back foot wraps around the branch and stretches the front of the body forward. Thus, the inchworm moves by controlling the front and back feet and by contracting and extending its body.

Inspired by inchworms, a biomimetic soft robot was designed based on the different friction forces of the tail and head, which could be excited by NIR light (Fig. 5(a)). As shown in Fig. 5(b), the soft robot consists of two reverse-connected GO/LDPE actuators. In the initial state, the contact angle between the head and the ground is much larger than that between the tail and the ground; hence, the friction force of the head is larger than that of the tail. When the NIR light hits

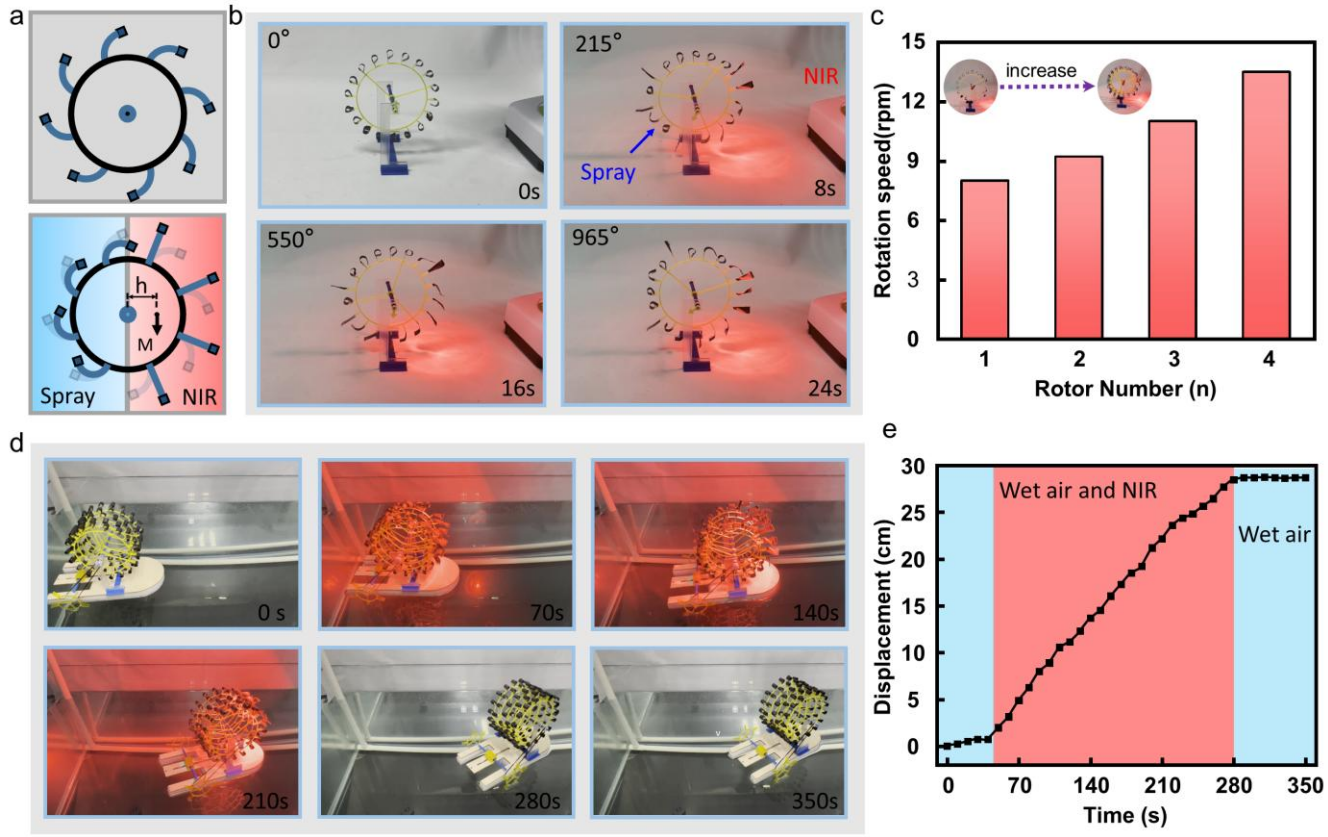

Fig. 6. Rotating robot based on GO/LDPE actuators. (a) Rotor relies on gravity to achieve rotational motion under the costimulation of humidity and NIR light. (b) Rotating process of the rotating robot with a rotor. (c) Relationship between the rotational speed of the rotating robot and the number of rotors. (d) Movement experiment of the rotating robot driving a boat. (e) Relationship between boat displacement and time.

the head of the robot, the body of the robot expands, and the robot moves the tail first due to the high friction of the head. When the angle of the head decreases to a certain extent, the friction force decreases, but the area of the tail increases. At this point, the friction of the tail is greater than that of the head, and the head of the robot moves forward until the robot is nearly flat. When the NIR light is turned off, the head of the robot deforms greatly and recovers first, the angle increases, and the robot moves forward to recover to the initial state. Therefore, by repeating the above actions, the soft robot can perform directional crawling. Fig. 5(c) shows the motion process of the robot crawling in one cycle. The motion process of the robot was basically consistent with the theoretical analysis, and its movement distance reached 4 mm (Movie S1). In addition, to verify the wide adaptability of the biomimetic robot, a crawling experiment was carried out to simulate the living environment of the inchworm. As shown in Fig. 5(d), the biomimetic robot was able to perform normal crawling similar to an inchworm on a leaf (Movie S2).

Since the traditional robotic gripper has fast response speed, high precision, and high repeatability and can achieve stable grasping for large weight and volume items, it has been widely used in industrial production, aerospace, position exploration, and other aspects[58]. However, due to the existing problems of traditional grasping devices, such as large volumes, high costs, and difficulty in grasping easily damaged or easily deformed objects[59], they may struggle to adapt to the needs of new developments. The soft matter–based gripper solves these problems neatly. Learning from nature and inspired by hawk claws, a biomimetic adaptive gripper based on multiple controls was designed to grasp objects (Fig. 5(e)). The GO/LDPE gripper can bend quickly under the stimulation of high humidity to successfully grasp and move a Styrofoam ball, and the release of the gripper can be achieved by reducing humidity or NIR light stimulation (Fig. 5(f)). This design shows the collaborative response to light and humidity stimuli. In addition, as shown in Fig. 5g, due to the soft characteristics of the biomimetic gripper, it can grasp objects of different shapes, such as balls, flowers, and capsules (Movie S3-4). These application scenarios demonstrate the adaptive ability and huge development potential of the biomimetic gripper.

The movement modes of natural creatures are mainly walking, swimming, jumping, flying, and so on. However, in human society, many devices rotate, such as machine tools, cars, and windmills. Based on the compatibility of traditional equipment, inspired by rotary mechanisms with blades, such as water wheels and windmills, a robot with a rotating motion mode was developed. By integrating multiple GO/LDPE actuators on the rotor, the rotary actuation of the robot can be realized by utilizing the centroid deviation of heavy objects under different position stimulations.

As shown in Fig. 6(a), in the initial state, the actuators on the rotor are not stimulated by external stimuli and remain in a stable state. The center of mass does not shift, and the rotor remains stationary. When the actuators on the rotor are stimulated by humidity on the left side and NIR light on the right side, the left actuators drive inward weight contraction, and the right actuators drive outward weight relaxation. These phenomena cause the center of mass deviation of the rotor and generate torque under the action of gravity to achieve rotational motion. Fig. 6(b) shows the motion process of the rotating robot. Under the synergistic stimulation of NIR light and humidity, the rotating robot rotated at 965° in 24 s.

The rotating robot can also increase the rotation speed or output torque by connecting the rotors in parallel. Fig. 6(c) shows the relationship between the number of rotors and the speed. With an increase in the number of rotors, the rotational speed of the rotating robot also increases significantly, up to 13.5 rpm (Movie S5). In addition, the robot with four rotors rotates more smoothly and has a better scope of application. Therefore, we selected the five-rotor-based robot to act as the engine module, driving a boat to move, to verify the practicality of the rotary robot. Fig. 6(d) shows snapshots of the rotating robot driving a boat. Under the synergistic control of infrared light and humidity, the rotating robot drove the boat to move 28 cm in 220 s (Fig. 6(e)), demonstrating the significant power output of the rotating robot (Movie S6). Therefore, the rotating robot could serve as an engine module to power small boats, which would decrease dependence on fossil fuels and promote the use of clean energy sources.

Conclusions

In summary, we used a simple solution evaporation method to fabricate a series of GO/LDPE actuators. The binding force between the GO layer and the LDPE layer is enhanced through the plasma treatment of LDPE films, which improves the mechanical stability of the GO/LDPE actuator. The initial state of the actuator can be adjusted by controlling the heating temperature and time to adapt to different application scenarios. In addition, the application of GO and LDPE, as different types of sensitive units, gives the actuator strong humidity response and photothermal response characteristics, respectively. The prepared film actuator is very sensitive to humidity and NIR light. The GO/LDPE actuator can quickly move from a curled state to a flat state at a light intensity of 40 mW cm^{-2}, with an angle change of approximately 500°. In addition, the actuator also showed a rapid response (~2.6 s) and large deformation (500°) under humidity stimulation. On this basis, to demonstrate the excellent performance of the actuator, we assembled an inchworm crawling robot and an adaptive soft gripper as proof of concept. The inchworm crawling robot could imitate inchworms crawling on leaves when stimulated by NIR light; the adaptive soft gripper could grasp, move, and release objects of different shapes, including pellets, flowers, and capsules, under multiple stimulations of humidity and NIR light. Moreover, to demonstrate the actuator's cooperative response advantages in terms of humidity stimulation and photothermal stimulation, a smart rotary robot was fabricated. It can be synergistically stimulated by humidity and infrared light to achieve rapid rotation, driving the boat to move. This work provides valuable guidance not only for the design and development of emerging intelligent responsive actuators but also for potential applications in artificial muscles, soft robots, energy conversion devices, biomimetic robots, and other fields.

3. Experimental section

3.1 Materials

GO was purchased from Shenzhen Shensui Technology Co., Ltd. and had a diameter of 1–10 μm. The oxygen content of GO is more than 42%; lauryl sodium sulfate (SDS) was purchased from Sinopharm Chemical Reagent Co., Ltd. Commercial LDPE film was purchased from Hanbang Plastic Packaging Store.

3.2 Preparation of GO solution

An aqueous SDS solution with a mass fraction of 0.02% was prepared using deionized water and SDS. Then, 10 mg, 20 mg, 40 mg, 60 mg, 80 mg, and 100 mg of GO were added to a 6 ml aqueous solution of SDS and ultrasonicated for 20 minutes to obtain different concentrations of GO solution.

3.3 Preparation of the LDPE film

The LDPE film was put into an oxygen plasma cleaner with the power set to 100 W and oxygen flow set to 30 sccm. After five minutes of treatment, an LDPE film with hydrophilic properties was acquired.

3.4 Preparation of GO/LDPE actuator

First, the LDPE film with hydrophilic properties was fixed in a Petri dish. Then, the prepared GO solution was cast on the LDPR film. The petri dish was placed in a fume hood to dry naturally. Finally, the film was peeled off to obtain the GO/LDPE actuator. By controlling the concentration and volume of the GO solution, actuators with different GO contents were obtained, which were 6.7 wt%, 12.5 wt%, 22.2 wt%, 30 wt%, 36.4 wt%, and 41.7 wt%. Finally, the GO/LDPE film was cut into 10 mm×30 mm rectangles for use.

3.5 Heat treatment of GO/LDPE actuator

The GO/LDPE film was clamped with two slides and heat treated with a graphene heating plate. By controlling the heating temperature and time, different bending angles can be obtained for the GO/LDPE actuators.

3.6 Characterizations and measurement

The surface and cross-sectional morphology of the GO/LDPE actuator was observed using a Quattro environmental scanning electron microscope. The thicknesses of the actuators with different GO contents were measured using a KH-7700 digital microscope. The hydrophilic modification of the LDPE film was carried out on a FEMTO plasma cleaner. The element distributions of GO and LDPE are characterized using EDAX-Element-C2B. The uniaxial tensile tests were performed on a 1ST Universal Test Machine (Tinius Olsen) at a cross-head speed of 100 mm min^{-1}. FT-IR spectra of GO and LDPE were characterized by a Thermo Scientific Nicolet iS50. NIR light was generated by an R95E Philips light source, and the light intensity was calibrated by the LIN-122 optical power meter at different distances. The controlled humidity gradient was created using a humidifier and dry nitrogen. The temperature and humidity of the experimental environment were measured using a UT333 thermohygrometer. The experimental images were recorded using an iPhone 13.

Author contributions

Yiwei Zhang: Validation, Formal analysis, investigation, writing - original draft, writing - review & editing, visualization. Ruiqian Wang: conceptualization, formal analysis, writing - review & editing. Wenjun Tan: formal analysis, resources. Lianchao Yang: investigation, resources. Xiaolong Lv: investigation, resources. Xiaodong Wang: investigation, resources. Feifei Wang: supervision, investigation. Chuang Zhang: conceptualization, supervision, project administration, funding acquisition.

Conflicts of interest

The authors declare that there is no conflict of interest regarding the publication of this article.

Acknowledgments

This work was supported by the National Natural Science Foundation of China [62003338, 61925307 and 62127811], the National Defense Science and Technology Innovation Key deployment project of Chinese Academy of Sciences [JCPYJJ-22020], the Youth Innovation Promotion Association, Chinese Academy of Science [2023210] and the Nature Foundation of Liaoning Province of China [2021-BS-021].

Notes and references

1. J. Z. Fan, S. Q. Wang, Q. G. Yu and Y. H. Zhu, *Soft Robot.*, 2020, **7**, 615-626.
2. B. Sun, Y. Z. Long, S. L. Liu, Y. Y. Huang, J. Ma, H. D. Zhang, G. Z. Shen and S. Xu, *Nanoscale*, 2013, **5**, 7041-7045.
3. Y. H. Chen, J. J. Yang, X. Zhang, Y. Y. Feng, H. Zeng, L. Wang and W. Feng, *Mater. Horiz.*, 2021, **8**, 728-757.
4. M. Li, A. Pal, A. Aghakhani, A. Pena-Francesch and M. Sitti, *Nat. Rev. Mater.*, 2022, **7**, 235-249.
5. B. Shin, J. Ha, M. Lee, K. Park, G. H. Park, T. H. Choi, K. J. Cho and H. Y. Kim, *Sci. Robot.*, 2018, **3**, eaar2629.
6. Y. He, K. R. Kong, Z. X. Guo, W. F. Fang, Z. Q. Ma, H. H. Pan, R. K. Tang and Z. M. Liu, *Adv. Funct. Mate.r*, 2021, **31**, 2101291.
7. X. Q. Wang, K. H. Chan, Y. Cheng, T. P. Ding, T. T. Li, S. Achavananthadith, S. Ahmet, J. S. Ho and G. W. Ho, *Adv. Mater.*, 2020, **32**, 2000351.
8. X. K. Dong, S. Kheiri, Y. N. Lu, Z. Y. Xu, M. Zhen and X. Y. Liu, *Sci. Robot.*, 2021, **6**, eabe3950.
9. L. Tang, L. Wang, X. Yang, Y. Y. Fen, Y. Li and W. Feng, *Prog. Mater. Sci.*, 2021, **115**, , 100702.
10. W. X. Fan, C. Y. Shan, H. Y. Guo, J. W. Sang, R. Wang, R. R. Zheng, K. Y. Sui and Z. H. Nie, *Sci. Adv.*, 2019, **5**, eaav7174.
11. C. Staudinger, M. Strobl, J. Breininger, I. Klimant and S. M. Borisov, *Sens. Actuators, B*, 2019, **282**, 204-217.
12. Q. Sun, C. Ayela and D. Thuau, *Adv. Mater. Interfaces* **8**, 2201349.
13. J. K. Ko, C. Kim, D. Kim, Y. Song, S. Lee, B. Yeom, J. Huh, S. Han, D. Kang, J. S. Koh and J. Cho, *Sci. Robot.*, 2022, **7**, eabo6463.

14. R. Q. Wang, C. Zhang, W.J. Tan, J. Yang, D. J. Lin and L. Q. Liu, *soft robot.*, 2023, **10**, 119-128.
15. C. Tang, B. Y. Du, S. W. Jiang, Q. Shao, X. G. Dong, X. J. Liu and H. C. Zhao, *Sci. Robot.*, 2022, **7**, eabm8597.
16. Y. Y. Xiao, Z. C. Jiang, J. B. Hou, X. S. Chen and Y. Zhao, *Soft Matter*, 2022, **18**, 4850-4867.
17. T. Gwisai, N. Mirkhani, M. G. Christiansen, T. T. Nguyen, V. Ling and S. Schuerle, *Sci. Robot.*, 2022, **7**, eabo0065.
18. Y. Kim and X. H. Zhao, *Chem. Rev.*, 2022, **122**, 5317-5364.
19. C. Huang, Z. Lai, X. Wu and T. Xu, *Cyborg Bionic Syst.*, 2022, **2022**, 0004.
20. M. T. Wang, Q. C. Li, J. X. Shi, X. Y. Cao, L. Z. Min, X. F. Li, L. L. Zhu, Y. H. Lv, Z. Qin, X. Y. Chen and K. Pan, *Acs Appl. Mater. Interfaces*, 2020, **12**, 33104-33112.
21. Y. Dong, L. Wang, N. Xia, Y. Wang, S. J. Wang, Z. X. Yang, D. D. Jin, X. Z. Du, E. W. Yu, C. F. Pan, B. F. Liu and L. Zhang, *Nano Energy*, 2021, **88**, 106254.
22. B. Han, Y. Y. Gao, Y. L. Zhang, Y. Q. Liu, Z. C. Ma, Q. Guo, L. Zhu, Q. D. Chen and H. B. Sun, *Nano Energy*, 2020, **71,** 104578.
23. Y. F. Chen, H. C. Zhao, J. Mao, P. Chirarattananon, E. F. Helbling, N. S. P. Hyun, D. R. Clarke and R. J. Wood, *Nature*, 2019, **575**, 324-329.
24. T. T. Vo-Doan, V. T. Dung and H. Sato, *Cyborg Bionic Syst.*, 2022, **2022**, 9780504.
25. G. R. Li, X. P. Chen, F. H. Zhou, Y. M. Liang, Y. H. Xiao, X. Cao, Z. Zhang, M. Q. Zhang, B. S. Wu, S. Y. Yin, Y. Xu, H. B. Fan, Z. Chen, W. Song, W. J. Yang, B. B. Pan, J. Y. Hou, W. F. Zou, S. P. He, X. X. Yang, G. Y. Mao, Z. Jia, H. F. Zhou, T. F. Li, S. X. Qu, Z. B. Xu, Z. L. Huang, Y. W. Luo, T. Xie, J. Gu, S. Q. Zhu and W. Yang, *Nature*, 2021, **591**, 2697-2699.
26. C. Zhang, Y. Zhang, W. Wang, N. Xi and L. Liu, *Cyborg and Bionic Systems*, 2022, **2022**, 9780504.
27. J. D. W. Madden, N. A. Vandesteeg, P. A. Anquetil, P. G. A. Madden, A. Takshi, R. Z. Pytel, S. R. Lafontaine, P. A. Wieringa and I. W. Hunter, *IEEE J. Oceanic Eng.*, 2004, **29**, 706-728.
28. L. Hines, K. Petersen, G. Z. Lum and M. Sitti, *Adv. Mater.*, 2017, **29**, 706-728.
29. Q. L. Zhao, Y. L. Wang, H. Q. Cui and X. M. Du, *J. Mater. Chem. C*, 2019, **7**, 6493-6511.
30. A. H. Cavusoglu, X. Chen, P. Gentine and O. Sahin, *Nat. Commun.*, 2017, **8**, 617.
31. T. Yang, H. L. Yuan, S. T. Wang, X. H. Gao, H. H. Zhao, P. Y. Niu, B. B. Liu, B. Li and H. J. Li, *J. Mater. Chem. A*, 2020, **8**, 19269-19277.
32. J. M. Christie and A. S. Murphy, *Am. J. Bot.*, 2013, **100**, 35-46.
33. G. Jekely, *Philos T. R. Soc. B*, 2009, **364**, 2795-2808.
34. E. Reyssat and L. Mahadevan, *J. R. Soc. Interface*, 2009, **6**, 951-957.
35. J. Dawson, J. F. V. Vincent and A. M. Rocca, *Nature*, 1997, **390**, 668-668.
36. A. Yanez, I. Desta, P. Commins, M. Magzoub and P. Naumov, *Adv. Biosyst.*, 2018, **2**.
37. R. Elbaum, L. Zaltzman, I. Burgert and P. Fratzl, *Science*, 2007, **316**, 884-886.
38. F. Gong, H. Li, J. Huang, Y. Jing, Z. Hu, D. Xia, Q. Zhou and R. Xiao, *Nano Energy*, 2022, **91**, 106677.
39. Y. Hu, L. L. Yang, Q. Y. Yan, Q. X. Ji, L. F. Chang, C. C. Zhang, J. Yan, R. R. Wang, L. Zhang, G. Wu, J. Sun, B. Zi, W. Chen and Y. C. Wu, *Acs Nano*, 2021, **15**, 5294-5306.
40. Y. Dong, J. Wang, X. K. Guo, S. S. Yang, M. O. Ozen, P. Chen, X. Liu, W. Du, F. Xiao, U. Demirci and B. F. Liu, *Nat. Commun.*, 2019, **10**, 4087.
41. D. R. Dreyer, S. Park, C. W. Bielawski and R. S. Ruoff, *Chem. Soc. Rev.,* 2010, **39**, 228-240.
42. H. H. Cheng, F. Zhao, J. L. Xue, G. Q. Shi, L. Jiang and L. T. Qu, *Acs Nano*, 2016, **10**, 9529-9535.
43. C. J. Yu, Z. Duan, P. X. Yuan, Y. H. Li, Y. W. Su, X. Zhang, Y. P. Pan, L. L. Dai, R. G. Nuzzo, Y. G. Huang, H. Q. Jiang and J. A. Rogers, *Adv. Mater.*, 2013, **25**, 1541-1546.
44. Z. J. Wang, C. Y. Li, X. Y. Zhao, Z. L. Wu and Q. Zheng, *J. Mater. Chem. B,* 2019, **7**, 1674-1678.
45. J. Yan, Y. M. Xia, J. J. Lai, C. X. Zhao, D. Xiang, H. Li, Y. P. Wu, Z. Y. Li and H. W. Zhou, *Macromolecular Mater. Eng.*, 2022, **307**, 2100765.
46. X. Y. Fan, H. L. Chen, Y. Zheng, Y. D. Liu, Q. Chen, X. Y. Li, Z. G. Gao, S. G. Li and M. J. Ma, *IEEE J. Sel. Top. Quantum Electron.*, 2023, **29**, 5600106.
47. V. Miskovic, E. Malafronte, C. Minetti, H. Machrafi, C. Varon and C. S. Iorio, *Front. Bioeng. Biotech.*, 2022, **10**, 806362.
48. Y. C. Wang, J. Q. Liu and S. Yang, *Appl. Phys. Rev.*, 2022, **9**, 011301.
49. L. Chen, M. Weng, P. Zhou, L. Zhang, Z. Huang and W. Zhang, *Nanoscale*, 2017, **9**, 9825-9833.
50. X. J. Luo, L. L. Li, H. B. Zhang, S. Zhao, Y. Zhang, W. Chen and Z. Z. Yu, *ACS Appl. Mater. Interfaces*, 2021, **13**, 45833-45842.
51. D. T. Zhang, K. Yang, X. Y. Liu, M. Luo, Z. Li, C. Z. Liu, M. Li, W. M. Chen and X. Y. Zhou, *Chem. Eng. J.*, 2022, **450,** 138013.
52. L. Torrisi, M. Cutroneo, V. Havranek, L. Silipigni, B. Fazio, M. Fazio, G. Di Marco, A. Stassi and A. Torrisi, Vacuum, 2019, **160**, 1-11.
53. J. N. Ma, Y. L. Zhang, D. D. Han, J. W. Mao, Z. D. Chen and H. B. Sun, Natl, Sci, Rev, 2020, **7**, 775-785.
54. T. Kawai, H. Kamio, T. Kondo and K. Kon-No, J. Phys. Chem. B, 2005, **109**, 4497-4500.
55. H. Rajandas, S. Parimannan, K. Sathasivam, M. Ravichandran and L. S. Yin, Polym. Test., 2012, **31**, 1094-1099..
56. S. Wang, Y. Gao, A. R. Wei, P. Xiao, Y. Liang, W. Lu, C. Y. Chen, C. Zhang, G. L. Yang, H. M. Yao and T. Chen, Nat. Commun., 2020, **11**, 4359.
57. D. A. Dikin, S. Stankovich, E. J. Zimney, R. D. Piner, G. H. B. Dommett, G. Evmenenko, S. T. Nguyen and R. S. Ruoff, *Nature*, 2007, **448**, 457-460.
58. L. Zhou, L. L. Ren, Y. Chen, S. C. Niu, Z. W. Han and L. Q. Ren, *Adv. Sci.*, 2021, **8**, 2002017.
59. J. Shintake, V. Cacucciolo, D. Floreano and H. Shea, *Adv. Mater.*, 2018, **30**, 1707035.

